

# Hydrogen Detection Using a Functionalized Photonic Crystal Vertical Cavity Laser

Benjamin G. Griffin, *Student Member, IEEE*, Amir Arbabi, *Student Member, IEEE*,  
 Ansas M. Kasten, *Student Member, IEEE*, Kent D. Choquette, *Fellow, IEEE*,  
 and Lynford L. Goddard, *Senior Member, IEEE*

(Invited Paper)

**Abstract**—A thin layer of palladium (Pd) was deposited on the surface of an etched air hole photonic crystal (PhC) vertical cavity surface emitting laser (VCSEL) to form a hydrogen gas ( $H_2$ ) sensor.  $H_2$  reacts with Pd, forming  $PdH_x$ , which induces a shift in the complex refractive index. With Pd on its surface, the reflectivity of the top distributed Bragg reflector depends on the  $H_2$  concentration. We present device operation theory and experimental results showing a 60% output power increase and a 52 pm redshift of the lasing wavelength at 4%  $H_2$ . Since the PhC VCSEL laser is single mode and the wavelength shift is comparable to the laser linewidth, the sensor can provide an accurate quantification of the  $H_2$  concentration over the range of 0–4%  $H_2$ .

**Index Terms**—Laser sensors, photonic crystals, vertical cavity surface emitting lasers.

## I. INTRODUCTION

SINCE the industrial revolution, fossil fuels have been used extensively to pave the way for advancements in science and technology. However, their nonrenewable nature will inevitably lead to a worldwide shortage in the foreseeable future. Additionally, the combustion products of our fossil fuel economy pollute the environment. As a result, a variety of alternative fuel sources are being actively pursued. Of these alternatives, hydrogen fuel cells show considerable promise due to the Earth's virtually unlimited supply of hydrogen gas ( $H_2$ ) and relatively neutral impact on the environment. However, due to the lower flammability limit of 4%  $H_2$  in air at 1 atm pressure [1], reliable sensors capable of quickly detecting small concentrations of  $H_2$  are a necessity.

The most common types of  $H_2$  sensors in use today include electrochemical sensors, metal oxide (MOX) sensors, pellistor-type combustible sensors, thermal conductivity sensors, and optical sensors [2]. Electrochemical  $H_2$  sensors can be divided into three main classes including amperometric, potentiometric, and conductometric sensors. These sensors have different

modes of operation, but essentially involve several electrodes submerged in an electrolyte while a current is passed between these electrodes in relation to the target gas concentration [3]. Although these sensors are a mature technology and sufficiently sensitive to  $H_2$ , they are often expensive and large, and exhibit relatively poor selectivity to other gases. Other commonly used sensors in the field also possess a variety of trade-offs. A popular material that is both highly sensitive and highly selective to  $H_2$  is Palladium (Pd). Pd is well known to react to  $H_2$ , forming  $PdH_x$  [4]. As it undergoes this phase transition, it experiences a shift in both the real and imaginary parts of its complex index of refraction. Additionally, it experiences a shift in its electrical conductivity, and so it is used in some metallic resistor sensors [5]. Pd is a safe material and can be used for repeated measurements since  $PdH_x$  returns to its original Pd state in the absence of  $H_2$ . Interestingly, Pd is capable of absorbing up to 900 times its volume in  $H_2$  [1]. A variety of new sensor technologies make use of Pd for  $H_2$  detection, including microelectromechanical systems (MEMS) involving a cantilever design [6], [7], nanowires that detect a shift in electrical resistance [8], [9], and deposition of Pd on an optical fiber to take advantage of the shifting optical properties [10]–[13]. The sensor presented in this paper uses a layer of palladium integrated into an active optical device, exploiting the optical properties of  $PdH_x$ .

Vertical cavity surface emitting lasers (VCSELs) with two-dimensional photonic crystals (PhCs) integrated on the surface have exhibited single-mode operation at a variety of operating wavelengths [14]–[18]. This single mode behavior in PhC VCSELs is useful for applications including optical communications [19], short-range optical interconnects [20], and optical storage [21]. The effective mode index of the PhC depends on the nature of the etched holes in the top DBR. Since modal confinement and top DBR reflectivity depend critically on the refractive indices and loss of the PhC material and the air within the etched holes, depositing a sensitive material into these holes should enable the adaptation of this PhC VCSEL design for general sensing applications.

PhC VCSELs with a thin layer of Pd deposited on the top DBR were fabricated and tested [22]. Here, we present device operation theory and a comparison to a standard, non-PhC VCSEL control sample with a thin layer of Pd deposited on the top DBR.

Manuscript received August 17, 2011; revised September 29, 2011; accepted September 29, 2011. Date of current version January 24, 2012. This work was supported in part by the National Science Foundation Award ID 0901388.

The authors are with the Department of Electrical and Computer Engineering, Micro and Nanotechnology Laboratory, University of Illinois at Urbana-Champaign, Urbana, IL 61801 USA (e-mail: griffi14@illinois.edu; arbabi1@illinois.edu; amkasten@gmail.com; choquett@illinois.edu; lgoddard@illinois.edu).

Color versions of one or more of the figures in this paper are available online at <http://ieeexplore.ieee.org>.

Digital Object Identifier 10.1109/JQE.2011.2171918

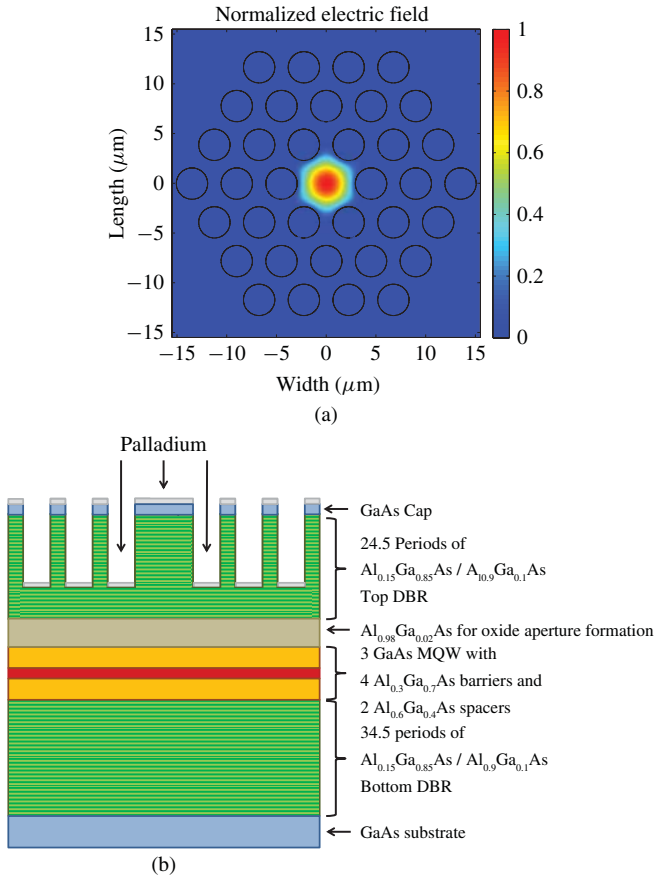


Fig. 1. (a) Top-down view of the PhC structure with the normalized electric field for the modeled PhC VCSEL. (b) Cross-section view of the layer structure through the center of the PhC pattern.

## II. SIMULATION SETUP

There are a variety of methods that have been used to model PhC VCSELs with varying degrees of accuracy [23], [24]. Here, the electric and magnetic field profiles for the PhC structure were calculated using the finite element method in COMSOL Multiphysics, and the mode matching techniques were used in MATLAB to convert these results into reflection and transmission coefficients at each interface. The modeling was done by considering each layer of the DBR as a separate two-dimensional domain. A top-down view of one of the two-dimensional layers showing the PhC structure and the normalized electric field is provided in Fig. 1(a), and a cross-section view of the entire modeled layer structure is provided in Fig. 1(b).

The top-most layer of the upper DBR is a 10 nm sheet of Pd with periodic air holes, and is defined by the Pd deposited on the surface of the device that did not fall into the etched holes. Since the dominant mode of the PhC VCSEL is centered almost entirely in the center defect of the PhC, this layer is modeled as a consistent, solid layer of Pd. This layer was simulated as the Pd without any  $H_2$  influence and then as the Pd after coming into contact with 4%  $H_2$  in  $N_2$ . The rest of the top DBR is comprised of two alternating concentrations of AlGaAs ( $Al_{0.15}Ga_{0.85}As$  and  $Al_{0.9}Ga_{0.1}As$ ), with a hexagonally ordered set of air holes surrounding a defect

in the center. The refractive index data for these layers at a wavelength of 850 nm (the lasing wavelength of the VCSEL) are  $n = 3.5298$  for the  $Al_{0.15}Ga_{0.85}As$  layer and  $n = 3.0627$  for the  $Al_{0.9}Ga_{0.1}As$  layer [25]. The air holes are etched 80% of the way through the top 24.5 pair DBR, and at the bottom of these air holes is a 10 nm layer of Pd. For the modeling of this particular 10 nm thick cross-section, the same two-dimensional PhC model is used, however, the air holes are replaced with solid Pd discs. Simulations were also done for both with and without  $H_2$ . The values for the refractive index of Pd at a wavelength of 850 nm in the absence of  $H_2$  are taken as  $n = 1.62$  and  $\kappa = 4.31$ , which are the values at 835 nm from [26]. After being exposed to 4%  $H_2$ , the new values for the refractive index are  $n = 1.45$  and  $\kappa = 3.86$  [26]. Underneath the air holes is the remaining 20% of the top DBR, and is comprised of solid layers of alternating AlGaAs concentrations.

After using COMSOL to produce the electric and magnetic field components for each of the two-dimensional domains, mode matching is performed at the interface between each layer, and optical coefficients are calculated for the entire DBR using the transmission matrix method as described in [27]. The mode matching is done by first normalizing the fields for each layer such that the electric and magnetic field components satisfy the relation

$$\frac{1}{2} \int (\mathbf{E}_1 \times \mathbf{H}_1) \cdot \hat{z} dS = \frac{1}{2} \int (\mathbf{E}_2 \times \mathbf{H}_2) \cdot \hat{z} dS = 1. \quad (1)$$

Then, the transmission matrix components at the interface of these two layers are determined by

$$T_{11} = T_{22} = \frac{1}{4} \int (\mathbf{E}_2 \times \mathbf{H}_1 + \mathbf{E}_1 \times \mathbf{H}_2) \cdot \hat{z} dS \quad (2a)$$

$$T_{12} = T_{21} = \frac{1}{4} \int (\mathbf{E}_2 \times \mathbf{H}_1 - \mathbf{E}_1 \times \mathbf{H}_2) \cdot \hat{z} dS. \quad (2b)$$

It should be noted that these equations only take the first order mode into consideration. In order to calculate the full transmission coefficients, the integral must be performed over all existing modes. However, assuming that the PhC VCSEL operates as a single mode device as it is designed, this approximation is valid.

The top DBR is treated as four distinct sections. The top section is the solid Pd layer. The next section includes 19 pairs of alternating AlGaAs concentrations with the PhC holes etched through. The transmission matrix for this section is computed by using the propagation constant for each section determined in COMSOL to calculate the propagation matrices, and the mode-matching technique to calculate the interface transmission matrices. All of these matrices are then multiplied together to produce a transmission matrix for this element of the top DBR. The next section contains the single layer where the Pd at the bottom of the etched holes is located. The transmission matrix for this layer is again computed using the mode matching technique using the COMSOL models with the Pd discs instead of the air holes. Finally, for the top DBR, the remaining 4.5 periods are solid AlGaAs layers, and are computed using the traditional transmission matrix technique for DBRs without the need for mode matching. The transmission matrices are then multiplied together to produce an overall transmission matrix for the top mirror. The

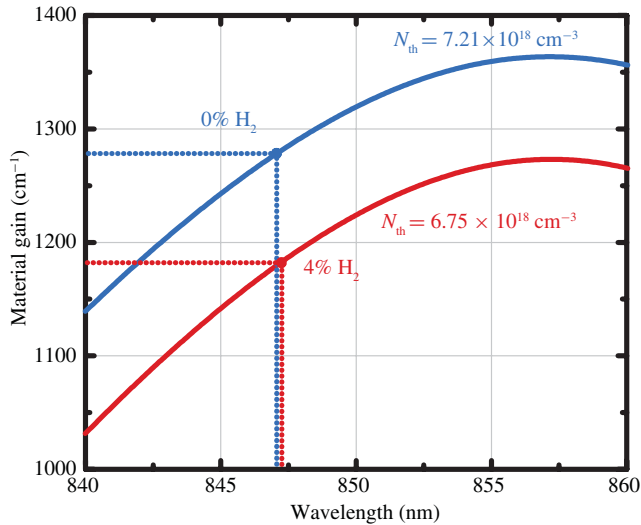


Fig. 2. Material gain curves of the two necessary carrier concentrations for threshold gain before and after exposure to 4%  $H_2$ . The threshold gain and lasing wavelength are indicated by the dotted lines.

entirety of the bottom DBR is computed using the traditional transmission matrix technique since the entire bottom DBR consists of simple, unpatterned layers. The reflection coefficient of the two mirrors can be easily determined from the final transmission matrices as  $T_{21}/T_{11}$ . The reflectivity of the top DBR is dependent on the Pd refractive index, so when  $H_2$  is added to the system, the reflectivity and phase of the top DBR will change, which will produce a shift in the wavelength to maintain the gain and the phase conditions for lasing.

The effective indices for the top DBR PhC layers with air holes are  $n = 3.5284$  for the  $Al_{0.15}Ga_{0.85}As$  layer and  $n = 3.0610$  for the  $Al_{0.90}Ga_{0.10}As$  layer. Since the mode is contained almost entirely within the defect, the refractive index of the air holes contributes very little to the effective index. Therefore, these effective index values are very close to the refractive indices of the solid layers. The bottom of the etched air holes is located within one of the  $Al_{0.90}Ga_{0.10}As$  layers. Therefore, the  $Al_{0.90}Ga_{0.10}As$  PhC layer with Pd discs instead of air holes is simulated with and without  $H_2$ . The effective index of this layer without  $H_2$  yields  $n = 3.0610$  and  $\kappa = 3.8547 \times 10^{-5}$ . With 4%  $H_2$ , the effective index is  $n = 3.0610$  and  $\kappa = 3.2315 \times 10^{-5}$ . The real component of these effective indices are nearly identical and are very close to the  $Al_{0.90}Ga_{0.10}As$  refractive index. The imaginary component, however, experiences a noticeable shift when in the presence of  $H_2$ .

A shift in both the reflection amplitude and phase is observed when  $H_2$  is introduced. This shift in reflection amplitude impacts the mirror loss of the device, which in turn shifts the threshold gain. For 3 GaAs multiple quantum wells (MQW) surrounded by  $Al_{0.3}Ga_{0.7}As$  barriers designed to lase at 850 nm, the gain curves for various carrier densities were computed at 330K, the expected temperature of the active region at threshold under continuous wave (CW) operation. Using the mirror loss for the cases with and without  $H_2$ , threshold gain coefficients are computed for these

TABLE I  
SIMULATION RESULTS FOR THE VCSEL SENSORS

Parameter	Symbol	Value
Top DBR Reflectivity (0% $H_2$ )	$R_1$	99.67%
Top DBR Reflectivity (4% $H_2$ )	$R_1$	99.72%
Bottom DBR Reflectivity	$R_2$	99.98%
Top DBR Phase (0% $H_2$ )	$\angle R_1$	$\pi - 0.0758$
Top DBR Phase (4% $H_2$ )	$\angle R_1$	$\pi - 0.0750$
Bottom DBR Phase	$\angle R_2$	$\pi - 0.0703$
Mirror Loss (0% $H_2$ )	$\alpha_m$	$22.8 \text{ cm}^{-1}$
Mirror Loss (4% $H_2$ )	$\alpha_m$	$20.4 \text{ cm}^{-1}$
Optical Confinement Factor	$\Gamma$	0.02565
Carrier Density (0% $H_2$ )	$N$	$7.21 \times 10^{18} \text{ cm}^{-3}$
Carrier Density (4% $H_2$ )	$N$	$6.75 \times 10^{18} \text{ cm}^{-3}$
Total Wavelength Shift	$\Delta\lambda$	21.6 pm

cases. For GaAs active material, the refractive index decreases with carrier density as  $dn/dN = -1.0 \times 10^{-20} \text{ cm}^3$  [28]. The shift in carrier density of the QW changes the optical path length of the cavity. This shift adds to the phase shift in the top DBR's reflectivity and produces a redshift in the peak wavelength when  $H_2$  is added. The gain spectrum was computed using SimuLase at several carrier densities and the gain and phase conditions were iteratively solved to determine the lasing wavelength and threshold carrier density. The gain spectrum at threshold at 0% and 4% is shown in Fig. 2.

### III. SIMULATION RESULTS

After performing the calculations on the full structure, an expected peak wavelength shift of 21.6 pm was found for 4%  $H_2$  in  $N_2$ . Table I shows this and the other results from the simulation. As shown, the top DBR reflectivity increases when exposed to  $H_2$ , which decreases the mirror loss, and leads to a redshift in the peak wavelength.

### IV. DEVICE FABRICATION

The PhC VCSEL was grown using metal-organic vapor phase epitaxy for lasing near 850 nm. The PhC was patterned using photolithography and was etched through 80% of the top DBR using inductively coupled plasma reactive ion etching. A detailed description of the geometry, fabrication, and testing of the non-functionalized devices can be found in [14]. After the VCSEL was fully fabricated and packaged, a 10 nm layer of Pd was deposited, allowing the Pd to be located at the top surface of the device as well as on the bottom of the etched air holes. As a control, another VCSEL of the same material and dimensions without the etched PhC was fabricated, and a layer of Pd was deposited on the top surface of its DBR. It was believed that the Pd at the bottom of the etched air holes of the PhC VCSEL should allow for a more significant overlap between the resonant mode and the Pd film, which would produce greater shifts in the output power and peak wavelength. Additionally, the single mode behavior from the PhC VCSEL was predicted to make shifts in the peak wavelength more noticeable. The control sample allows

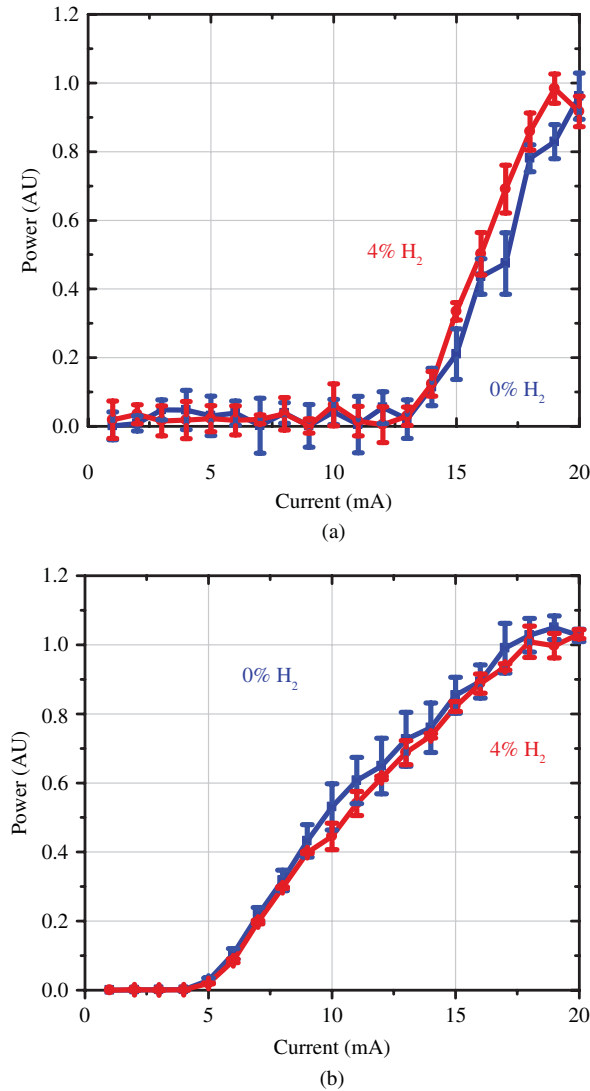


Fig. 3. L-I curves before and after soaking in 4% H<sub>2</sub> for an hour for the (a) PhC VCSEL and (b) standard VCSEL.

determination of what impact, if any, the surface coating of Pd on the top of the DBR has on the device's sensing properties.

## V. EXPERIMENTAL METHODS

The sensor was measured by sealing the VCSEL within a custom-machined polycarbonate chamber with a volume of 0.55 cm<sup>3</sup>. The leads of the packaged VCSEL were soldered to a printed circuit board with traces connecting to contact pads outside of the chamber. The light output from the VCSEL is coupled onto a fiber external to the chamber, which leads to an optical spectrum analyzer (OSA). The OSA used for these measurements was a Hewlett Packard 70951 B with the resolution set to 0.08 nm. During the measurements, a steady stream of 5000 sccm of N<sub>2</sub> is flowed, and small concentrations of H<sub>2</sub> are turned on and off as desired to monitor the change in optical properties. Output power is measured by integrating the measured spectrum from the OSA. Since the collection lens is located outside of the testing chamber, the sample cannot be

properly positioned at its appropriate focal point. Therefore, the magnitude of the power measurements was quite small. For comparison between the two samples, the data for the power measurements were normalized to unity at a current of 20 mA.

## VI. EXPERIMENTAL RESULTS

Initially, the laser spectrum was measured and the output power calculated as the current was increased, producing L-I curves for both a purely N<sub>2</sub> ambient, and an ambient containing some H<sub>2</sub>. Fig. 3 shows L-I curves for the PhC VCSEL and standard VCSEL before and after being soaked in 4% H<sub>2</sub> for an hour. Five runs were collected and averaged to check repeatability and determine error bars.

As shown, the PhC VCSEL experiences a statistically significant increase in output power and lasing efficiency after being exposed to H<sub>2</sub> while the standard VCSEL shows no noticeable change. Additionally, spectra were collected for both of these devices under exposures to a variety of H<sub>2</sub> concentrations. As shown in Fig. 3, for the PhC VCSEL with injection currents between 15–19 mA, the output power after being exposed to H<sub>2</sub> is larger than the power before being exposed to H<sub>2</sub>. The largest fractional power shift occurs near threshold. At 15 mA, a 60% power increase is observed for 4% H<sub>2</sub>. However, at 20 mA injection current, the power drops with H<sub>2</sub>. Thus, we investigate the output spectra in Fig. 4 at 15 mA and 20 mA after soaking the sensor in various H<sub>2</sub> concentrations for one hour each. The PhC VCSEL shows a single mode peak that redshifts by an almost constant amount for each increase of H<sub>2</sub> concentration, while the standard VCSEL shows multi-mode behavior with no discernible shift after H<sub>2</sub> exposure. Additionally, the PhC VCSEL spectra at 20 mA injection current follows the same trend regarding the output power as shown in Fig. 3.

Fig. 5 shows how the peak wavelength shifts as a function of injection current before and after H<sub>2</sub> exposure. The 130 pm/mA redshift seen in both devices is attributed to device heating. For the PhC VCSEL, there is a consistent redshift in peak wavelength with H<sub>2</sub> concentration for all injection currents. The run to run variation in the wavelength at fixed current and H<sub>2</sub> concentration for the PhC VCSEL is 2 pm, which is very small compared to the 52 pm wavelength shift for 4% H<sub>2</sub>. However, for the standard VCSEL, the two curves overlap, showing no significant shift in the peak wavelength for any injection current.

Next, time dependent H<sub>2</sub> pulse measurements were performed to observe the response and recovery time for the devices as they are injected with a constant current of 19 mA, where the absolute power shift is greatest. Both the output power and the spectrum were observed as varying concentrations of H<sub>2</sub> were pulsed on and off. The results from this study are shown in Figs. 6 and 7. For the PhC VCSEL, both power and wavelength begin to shift immediately as the H<sub>2</sub> is pulsed on and off, and typically takes about 2–5 minutes to fully saturate, depending on H<sub>2</sub> concentration. Additionally, the magnitude of the response scales with H<sub>2</sub> concentration, allowing for the concentration to be approximated by either

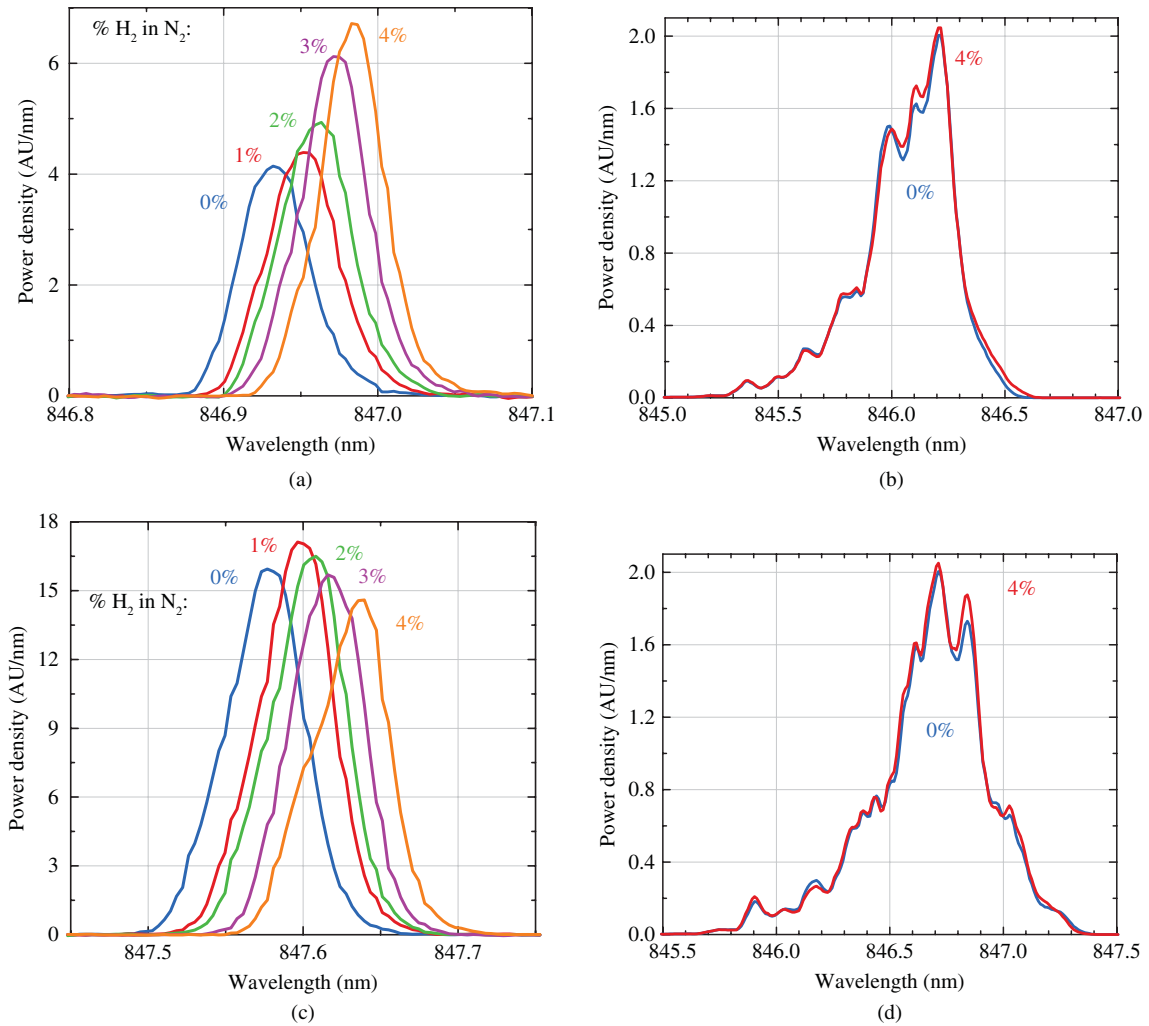


Fig. 4. Sensor spectra after soaking in various  $H_2$  concentrations for an hour each at 15 mA injection current for (a) PhC VCSEL and (b) standard VCSEL at 20 mA injection current for (c) PhC VCSEL and (d) standard VCSEL.

the power or wavelength shift. The standard VCSEL, however, shows no noticeable shift in either power or wavelength when exposed to  $H_2$ . The power measurement just shows steady noise while the wavelength measurement reveals mode-hopping.

## VII. DISCUSSION

From the simulation, two primary effects determine the theoretical wavelength shift. Since the device's lasing wavelength is determined by the gain and phase conditions, any shift in round trip gain or phase with the addition of  $H_2$  can lead to a wavelength shift. The phase condition depends on the phases of the top DBR, the bottom DBR, and the cavity. This condition is met when the sum of these three phases is equal to an integer multiple of  $2\pi$ . Since the bottom DBR's reflectivity and phase do not depend directly on the  $H_2$  concentration due to the lack of Pd integration, the phase in the top DBR and cavity are of the most importance. It should be noted that as the lasing wavelength shifts due to the  $H_2$  presence, so too does the phase of the bottom DBR. As shown in Table I, the phase of the top DBR increases when  $H_2$  is added to the

system. This effect alone is capable of producing a wavelength shift. Assuming that both the cavity phase and the bottom DBR phase are constant, the shift in the top DBR phase only yields a 2.5 pm redshift. However, the refractive index of the active material depends on the carrier density. Thus, the optical path length of the cavity depends on the reflectivity of the top and bottom DBRs, and so changing the reflectivity in the top DBR will impact the lasing wavelength produced from the gain condition. If the phase of the top and bottom DBRs are kept constant, and only the wavelength shift due to the change in optical path length of the cavity is considered, the lasing wavelength redshifts 18.6 pm. The total theoretical wavelength shift of 21.6 pm is due to both of these effects and their interaction; however, it is clear that the carrier density dependent refractive index of the active material is the more significant phenomenon.

The total wavelength shift from the simulation results is of the same order of as the experimental wavelength shift for the PhC VCSEL sensor. The experimental value for the shift at 4%  $H_2$  was about 2.4 times larger than the value predicted from the simulation. This discrepancy is likely due to inaccuracies in the model parameters. In particular, the refractive index values

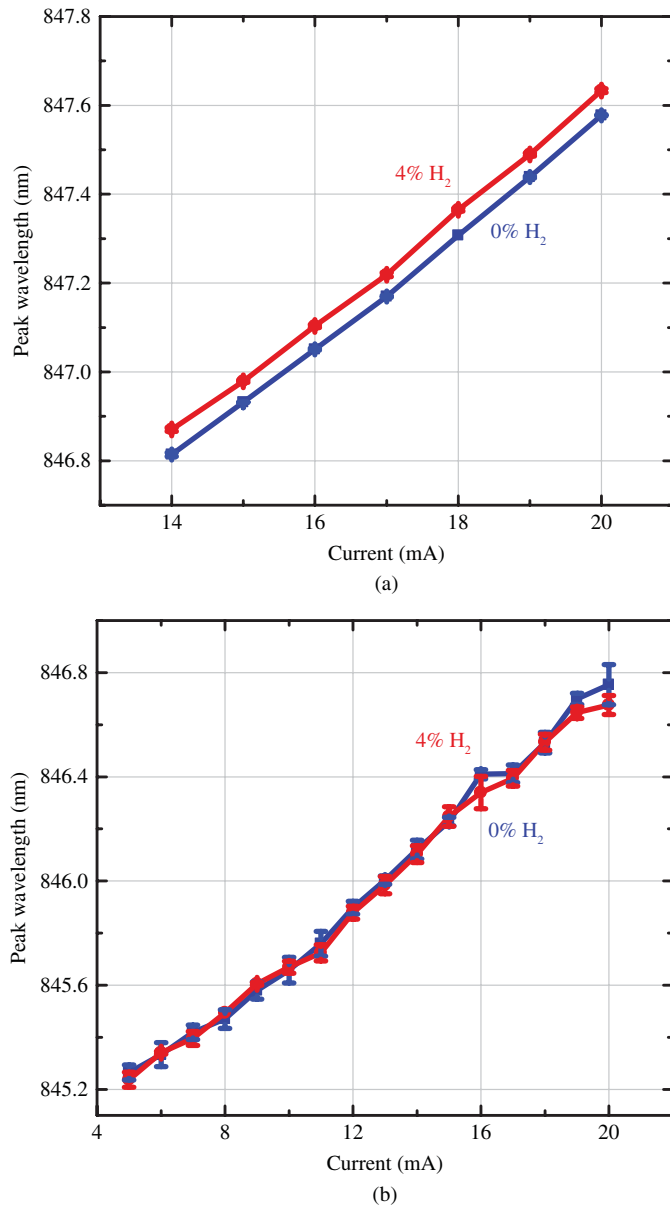


Fig. 5. Peak wavelength as a function of injection current for the (a) PhC VCSEL and (b) standard VCSEL.

of the Pd layer with and without H<sub>2</sub> are known to depend on the Pd thickness, porosity, and deposition conditions. The wavelength shift in the simulations is highly dependent on the Pd thickness and its refractive index shift after being introduced to H<sub>2</sub>. If the model's refractive indices before and after H<sub>2</sub> exposure are inaccurate, or if the experimentally deposited thickness has any variation, this will translate to significant alterations in the wavelength shift. Additionally, if the PhC holes are not etched perfectly straight, or if the experimentally deposited Pd is not deposited at exactly normal incidence, there will be a thin annular coating of Pd on the inside of the etched holes. Due to the very small penetration depth of the fundamental mode into the Pd holes, this very thin coating creates a much greater effective thickness of Pd within the PhC, which in turn causes a larger shift. Finally, from the experimental data, it is observed that as H<sub>2</sub> is introduced, the

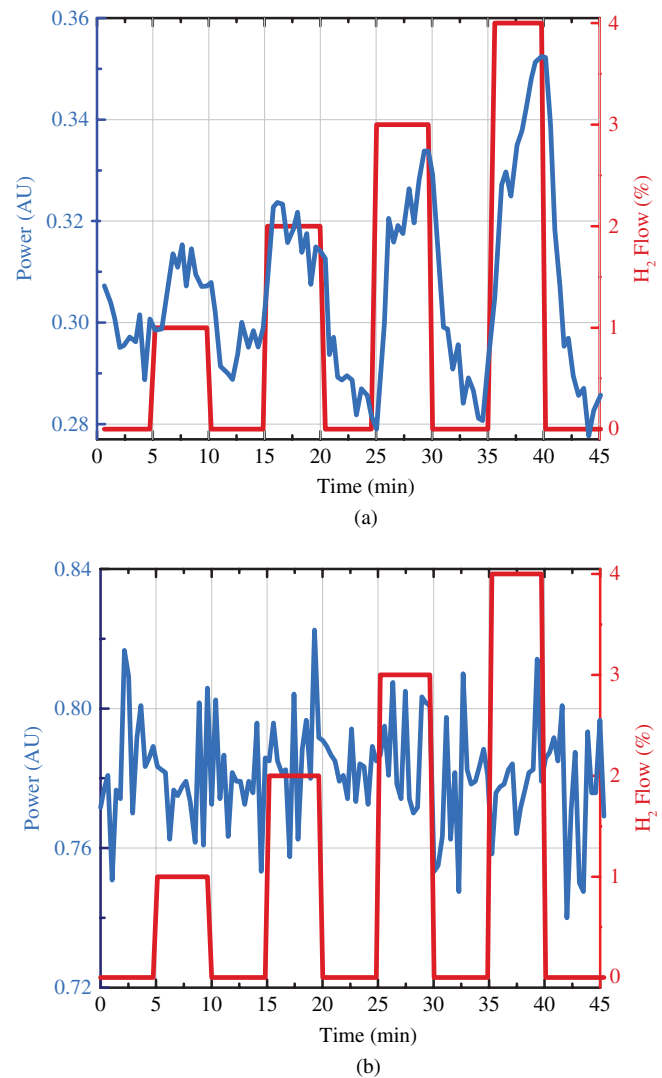


Fig. 6. Pulsed H<sub>2</sub> measurements measuring output power for the (a) PhC VCSEL and (b) standard VCSEL.

voltage across the device increases by an amount related to the H<sub>2</sub> concentration as the current is held constant. This suggests that as Pd absorbs H<sub>2</sub>, the resistance of the device increases. The conductance of Pd films generally decreases with H<sub>2</sub> [29]. Thus, the resistance of the PhC VCSEL top contact increases since some current spreads along the top most Pd layer. At 4% H<sub>2</sub>, the resistance increased by 0.3 Ω, which would heat the device by about 0.2 K and produce an additional redshift of about 5 pm. Small contributions from each of these potential inaccuracies can realistically explain the discrepancy between the theoretical and experimental models.

The wavelength and power shifts for the standard VCSEL were not visible for any concentration of H<sub>2</sub>; however, the PhC VCSEL shows very noticeable changes. This is believed to be primarily a result of the single mode nature of the PhC VCSEL. The multi-mode spectrum for the standard VCSEL makes it difficult to distinguish any measurable shift, but the single peak for the single mode PhC VCSEL moves consistently with H<sub>2</sub> concentration. Additionally, the Pd located at the bottom of the etched air holes in the PhC VCSEL

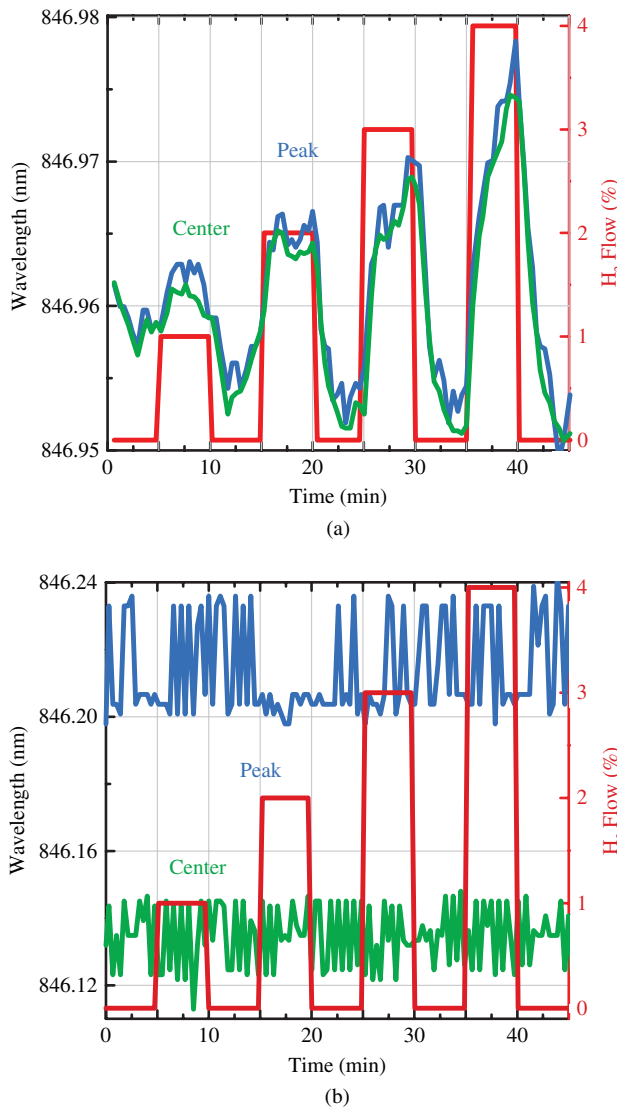


Fig. 7. Pulsed H<sub>2</sub> measurements measuring peak wavelength FWHM center for the (a) PhC VCSEL and (b) standard VCSEL.

contributes a small enhancement to the wavelength and power shifts. However, since most of the mode is concentrated in the PhC defect, only a very small portion of this mode overlaps the Pd in the holes.

As shown in Fig. 5(a), the peak wavelength shift for 4% H<sub>2</sub> appears to be independent of current. Therefore, a fit was performed on the peak wavelength shift,  $\Delta\lambda$  (in pm) versus the H<sub>2</sub> concentration percentage with data taken at 0, 1, 2, 3, and 4% H<sub>2</sub> and currents of 14–20 mA. A power law,  $\Delta\lambda = b(\text{H}_2\%)^c$  was used to capture the nonlinear behavior at low concentration. The fit produced  $b = 19.4 \pm 1.1$  and  $c = 0.727 \pm 0.050$ . Additionally, a 95% prediction interval can be applied to this set of data yielding an estimate of the range of expected wavelength shifts for any specified concentration of H<sub>2</sub>. Using the Hubaux and Vos method [30], an approximate value for the minimum detection limit (MDL) of the sensor is found to be 0.8% H<sub>2</sub>. This is calculated by finding the point in which the upper prediction limit intersects the y-axis, following this point horizontally to the lower prediction limit,

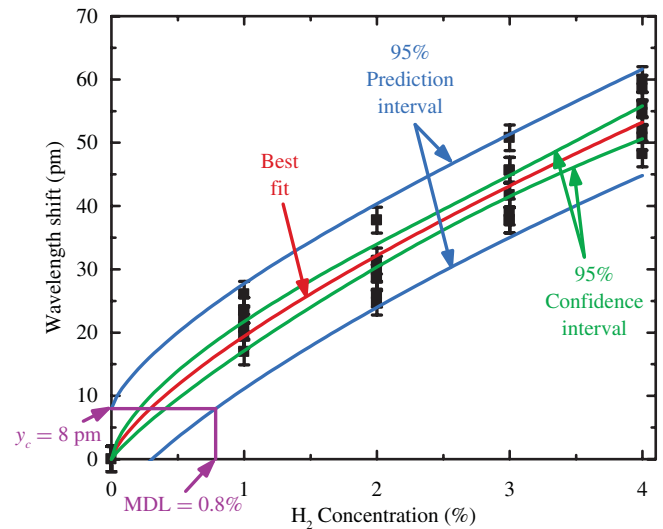


Fig. 8. Fitting parameters for the wavelength shift of the H<sub>2</sub> sensor including an approximate MDL of 0.8% H<sub>2</sub>.

and then proceeding vertically to the x-axis, which defines the MDL. The Hubaux and Vos method is typically applied to a linear regression; however, it is assumed that this method still produces a valid approximation for this nonlinear fit. The results from this fit and a graphical representation of how the MDL was calculated are shown in Fig. 8. This demonstrates that after calibration in an N<sub>2</sub> ambient, the peak wavelength shift can be used to accurately determine the H<sub>2</sub> concentration, independent of the sensor's injection current.

## VIII. CONCLUSION

In conclusion, a H<sub>2</sub> sensor utilizing a thin film of Pd deposited on the surface of a PhC VCSEL has been presented. This device produces consistent, repeatable shifts in both output power and wavelength as a function of H<sub>2</sub> concentration. At 15 mA injection current, near threshold, the sensor produces an increase in output power of about 60% at 4% H<sub>2</sub>. Additionally, the device produces a redshift in the peak wavelength independent of current of about 52 pm at 4% H<sub>2</sub>. By comparing this device to a standard VCSEL with Pd deposited on the top surface, it has been determined that the single mode nature of the PhC VCSEL is necessary to observe the H<sub>2</sub> induced changes in power and wavelength.

## REFERENCES

- [1] T. B. Flanagan and W. A. Oates, "The palladium-hydrogen system," *Annu. Rev. Mater. Sci.*, vol. 21, pp. 269–304, Aug. 1991.
- [2] W. J. Buttner, M. B. Post, R. Burgess, and C. Rivkin, "An overview of hydrogen safety sensors and requirements," *Int. J. Hydrogen Energy*, vol. 36, no. 3, pp. 2462–2470, 2011.
- [3] G. Korotcenkov, S. D. Han, and J. R. Stetter, "Review of electrochemical hydrogen sensors," *Chem. Rev.*, vol. 109, no. 3, pp. 1402–1433, Mar. 2009.
- [4] L. Schlapbach and A. Züttel, "Hydrogen-storage materials for mobile applications," *Nature*, vol. 414, no. 6861, pp. 353–358, Nov. 2001.
- [5] T. Hübert, L. Boon-Brett, G. Black, and U. Banach, "Hydrogen sensors – A review," *Sens. Actuat. B: Chem.*, vol. 157, no. 2, pp. 329–352, Oct. 2011.

- [6] S. V. Pham, L. J. Kauppinen, M. Dijkstra, H. A. G. M. van Wolferen, R. M. de Riddler, and H. J. W. M. Hoekstra, "Read-out of cantilever bending with a grating waveguide optical cavity," *IEEE Photon. Technol. Lett.*, vol. 23, no. 4, pp. 215–217, Feb. 2011.
- [7] D. R. Baselt, D. Fruhberger, E. Klaassen, S. Cemalovic, C. L. Britton, Jr., S. V. Patel, T. E. Mlsna, D. McCorkle, and B. Warmack, "Design and performance of a microcantilever-based hydrogen sensor," *Sens. Actuat. B: Chem.*, vol. 88, no. 2, pp. 120–131, Jan. 2003.
- [8] X. Q. Zeng, M. L. Latimer, Z. L. Xiao, S. Panuganti, U. Welp, W. K. Kwok, and T. Xu, "Hydrogen gas sensing with networks of ultrasmall palladium nanowires formed on filtration membranes," *Nano Lett.*, vol. 11, no. 1, pp. 262–268, Jan. 2011.
- [9] J.-S. Noh, J. M. Lee, and W. Lee, "Low-dimensional palladium nanostructures for fast and reliable hydrogen gas detection," *Sensors*, vol. 11, no. 1, pp. 825–851, 2011.
- [10] S. J. McKeown, B. G. Griffin, and L. L. Goddard, "Fiber optic hydrogen sensor utilizing facet-etched metal nano-apertures," in *Proc. 23rd Annu. Meet. IEEE Photon. Soc.*, Denver, CO, Nov. 2010, pp. 730–731.
- [11] C. Perrotton, N. Javahiraly, M. Slamman, H. Schreuders, B. Dam, and P. Meyrueis, "Optimization of Pd surface plasmon resonance sensors for hydrogen detection," *Proc. SPIE*, vol. 8065, pp. 80651F-1–80651F-5, Mar. 2011.
- [12] C. Lu-Jun, S. Hui-Chao, Z. Gang, Z. Ze-Xiang, and Z. Jun, "Optical fiber hydrogen sensor based on light reflection and a palladium-silver thin film," *Optoelectron. Lett.*, vol. 7, no. 4, pp. 249–252, 2011.
- [13] H. Liu, M. Yang, J. Dai, K. Cao, H. Liao, and P. Zhang, "Hydrogen sensor based on side-polished fiber Bragg gratings coated with thin palladium film," *Proc. SPIE*, vol. 7753, pp. 77538O-1–77538O-4, May 2011.
- [14] A. M. Kasten, M. P. Tan, J. D. Sulkin, P. O. Leisher, and K. D. Choquette, "Photonic crystal vertical cavity lasers with wavelength-independent single-mode behavior," *IEEE Photon. Technol. Lett.*, vol. 20, no. 23, pp. 2010–2012, Dec. 2008.
- [15] K. H. Lee, J. H. Baek, I. K. Hwang, Y. H. Lee, G. H. Lee, J. H. Ser, H. D. Kim, and H. E. Shin, "Square-lattice photonic-crystal vertical-cavity surface-emitting lasers," *Opt. Exp.*, vol. 12, no. 17, pp. 4136–4143, Aug. 2004.
- [16] H. P. D. Yang, F. I. Lai, Y. H. Chang, H. C. Yu, C. P. Sung, H. C. Kuo, S. C. Wang, S. Y. Lin, and J. Y. Chi, "Singlemode (SMSR > 40 dB) proton-implanted photonic crystal vertical-cavity surface-emitting lasers," *Electron. Lett.*, vol. 41, no. 6, pp. 326–328, Mar. 2005.
- [17] D. S. Song, S. H. Kim, H. G. Park, C. K. Kim, and Y. H. Lee, "Single-fundamental-mode photonic-crystal vertical-cavity surface-emitting lasers," *Appl. Phys. Lett.*, vol. 80, no. 21, pp. 3901–3903, May 2002.
- [18] H. J. Unold, M. Golling, R. Michalzik, D. Supper, and K. J. Ebeling, "Photonic crystal surface-emitting lasers: Tailoring waveguiding for single-mode emission," in *Proc. 27th Eur. Conf. Opt. Commun.*, vol. 4, Amsterdam, The Netherlands, Aug. 2001, pp. 520–521.
- [19] H. Hasegawa, Y. Oikawa, T. Hirooka, M. Yoshida, and M. Nakazawa, "10 Gb/s transmission over 3 km at 850 nm using single-mode photonic crystal fiber, single-mode VCSEL, and Si-APD," in *Proc. IEEE/OSA Opt. Fiber Commun. Conf.*, Anaheim, CA, Mar. 2006, pp. 1–3.
- [20] J. Bristow, J. Lehman, Y. Liu, M. Hibbs-Brenner, L. Galarneau, and R. Morgan, "Recent progress in short-distance optical interconnects," *Proc. SPIE*, vol. 3005, pp. 112–119, Feb. 1997.
- [21] M. Mansuripur and G. Sincerbox, "Principles and techniques of optical data storage," *Proc. IEEE*, vol. 85, no. 11, pp. 1780–1796, Nov. 1997.
- [22] B. G. Griffin, A. M. Kasten, K. D. Choquette, and L. L. Goddard, "Palladium-coated photonic crystal vertical cavity lasers for hydrogen sensing applications," in *Proc. 23rd Annu. Meet. IEEE Photon. Soc.*, Denver, CO, Nov. 2010, pp. 373–374.
- [23] H. Y. Ryu, H. G. Park, and Y. H. Lee, "2-D photonic crystal semiconductor lasers: Computational design, fabrication, and characterization," *IEEE J. Sel. Topics Quantum Electron.*, vol. 8, no. 4, pp. 891–908, Jul.–Aug. 2002.
- [24] M. Dems, I. S. Chung, P. Nyakas, S. Bischoff, and K. Panajotov, "Numerical methods for modeling photonic-crystal VCSELs," *Opt. Exp.*, vol. 18, no. 15, pp. 16042–16054, Jul. 2010.
- [25] S. Adachi, "GaAs, AlAs, and Al<sub>x</sub>Ga<sub>1-x</sub>As material parameters for use in research and device applications," *J. Appl. Phys.*, vol. 58, no. 3, pp. R1–R29, Aug. 1985.
- [26] P. Tobiska, O. Hugon, A. Trouillet, and H. Gagnaire, "An integrated optic hydrogen sensor based on SPR on palladium," *Sens. Actuat. B: Chem.*, vol. 74, no. 1, pp. 168–172, Apr. 2001.
- [27] J. Hong, W. Huang, and T. Makino, "On the transfer matrix method for distributed-feedback waveguide devices," *J. Lightw. Technol.*, vol. 10, no. 12, pp. 1860–1868, Dec. 1992.
- [28] J. G. Mendoza-Alvarez, F. D. Nunes, and N. B. Patel, "Refractive index dependence on free carriers for GaAs," *J. Appl. Phys.*, vol. 51, no. 8, pp. 4365–4367, Aug. 1980.
- [29] M. Ramanathan, G. Skudlarek, H. H. Wang, and S. B. Darling, "Crossover behavior in the hydrogen sensing mechanism for palladium ultrathin films," *Nanotechnology*, vol. 21, no. 12, pp. 125501-1–125501-6, Mar. 2010.
- [30] A. Hubaux and G. Vos, "Decision and detection limits for calibration curves," *Anal. Chem.*, vol. 42, no. 8, pp. 849–855, Jul. 1970.



**Benjamin G. Griffin** (S'06) received the B.S. degree in electrical engineering from Virginia Commonwealth University, Richmond, and the M.S. degree in electrical engineering from the University of Illinois at Urbana-Champaign, Urbana, in 2008 and 2010, respectively, where he is currently pursuing the Ph.D. degree with the Photonic Systems Laboratory.

His current research interests include design, fabrication, and characterization of photonic devices for trace chemical detection.

Mr. Griffin is a Student Member of the IEEE Photonics Society.



**Amir Arbabi** (S'06) was born in Malayer, Iran, in 1984. He received the B.Sc. degree in electrical engineering from the University of Tehran, Tehran, Iran, in 2006, and the M.Sc. degree in electrical engineering from the University of Waterloo, ON, Canada, in 2009. He is currently pursuing the Ph.D. degree in electrical engineering from the Department of Electrical and Computer Engineering, University of Illinois at Urbana-Champaign, Urbana.

He has been with the Photonic Systems Laboratory, University of Illinois at Urbana-Champaign,

as a Research Assistant since 2009. His current research interests include plasmonic and nanophotonic devices, fast numerical methods for simulation and design of novel photonic devices, and fundamental features and limits in optics and electromagnetics.

Mr. Arbabi was a recipient of the Ontario Graduate Scholarship and the President's Graduate Scholarship while at the University of Waterloo, and the Ernest A. Reid Fellowship Award at the University of Illinois at Urbana-Champaign. He is a Student Member of the Optical Society of America. He is a reviewer for the IEEE PHOTONICS JOURNAL and the *Progress in Electromagnetics Research journals*.



**Ansa M. Kasten** (S'07) received the Diploma degree in electrical engineering from the University of the Saarland, Saarbrücken, Germany, and the M.S. degree in electrical engineering from the University of Illinois at Urbana-Champaign, Urbana, in 2003 and 2006, respectively, where he is currently pursuing the Ph.D. degree with the Department of Electrical and Computer Engineering.

He was a Visiting Scholar with the Department of Agricultural Engineering, University of Illinois at Urbana-Champaign, from 2003 to 2004, where he later joined the Photonics Device Research Group. His current research interests include photonic devices such as vertical-cavity surface-emitting lasers (VCSELs), VCSEL arrays, detector arrays, photonic crystal VCSELs, and their integration into microfluidic systems for biomedical sensing applications.

Mr. Kasten is a Student Member of the Optical Society of America.



**Kent D. Choquette** (M'97–SM'02–F'03) received the B.S. degree in engineering physics and applied mathematics from the University of Colorado-Boulder, Boulder, and the M.S. and Ph.D. degrees in materials science from the University of Wisconsin-Madison, Madison.

He was a Post-Doctoral Researcher with the AT&T Bell Laboratories, Murray Hill, NJ, from 1990 to 1992. He then joined Sandia National Laboratories, Albuquerque, NM, and he was a Principal with Technical Staff Member, from 1993 to 2000. He

became a Professor in the Department of Electrical and Computer Engineering, University of Illinois at Urbana-Champaign, Urbana, in 2000. He has authored more than 200 technical publications and three book chapters, and has presented numerous invited talks and tutorials.

Prof. Choquette is a fellow of the Optical Society of America and the International Society for Optical Engineering. He was the recipient of the IEEE Lasers and Electro-Optics Society (LEOS) Engineering Achievement Award in 2008. He has served as an Associate Editor of the IEEE JOURNAL OF QUANTUM ELECTRONICS and the IEEE PHOTONIC TECHNOLOGY LETTERS, and as a Guest Editor of the IEEE JOURNAL OF SELECTED TOPICS IN QUANTUM ELECTRONICS. From 2000 to 2002, he was an IEEE/LEOS Distinguished Lecturer.



**Lynford L. Goddard** (S'04–M'05–SM'10) received the B.S. degree in mathematics and physics, the M.S. degree in electrical engineering, and the Ph.D. degree in physics from Stanford University, Stanford, CA, in 1998, 2003, and 2005, respectively.

He conducted post-doctoral research on photonic integrated circuits, sensors, and data processing systems with Lawrence Livermore National Laboratory, Livermore, CA, from 2005 to 2007. In 2007, he became an Assistant Professor with the Department of Electrical and Computer Engineering, University

of Illinois at Urbana-Champaign, Urbana. He is the author or co-author of over 70 publications. His current research interests include fabricating, characterizing, and modeling individual lasers and photonics-based sensors, instrumentation and integrated circuits, developing new processing techniques, and testing novel semiconductor materials and devices.

Dr. Goddard is an Associate Editor of the IEEE PHOTONICS JOURNAL, and a member of the Optical Society of America, the Society of Photo-Optical Instrumentation Engineers, the American Society for Engineering Education, and the American Association for the Advancement of Science (AAAS). He is the recipient of the Presidential Early Career Award for Scientists and Engineers, nominated by the Department of Energy in 2008 and the inaugural AAAS Early Career Award for Public Engagement with Science in 2011.